RESEARCH ARTICLE

TWOR: Improving Modeling and Self-Localization in RFID-Tag Networks Under Colored Noise

JORGE A. ORTEGA-CONTRERAS [ID], JOSÉ A. ANDRADE-LUCIO [ID], (Member, IEEE),
OSCAR G. IBARRA-MANZANO [ID], (Member, IEEE), AND YURIY S. SHMALIY [ID], (Fellow, IEEE)
Department of Electronic Engineering, Universidad de Guanajuato, Salamanca, Guanajuato 36855, Mexico
Corresponding author: Jorge A. Ortega-Contreras (ja.ortegacontreras@ugto.mx)

ABSTRACT This paper discusses the three-wheeled omnidirectional robot (TWOR) self-localization in radio frequency identification (RFID) tag environments. The nonlinear TWOR model is significantly improved by using geometric interpretation and incremental time representation in discrete time. The TWOR position and heading are self-estimated using distance measurements to RFID tags and a digital gyroscope in the presence of typical colored measurement noise (CMN). The extended unbiased finite impulse response (EFIR) is developed along with the extended Kalman filter (EKF) and their versions, cEKF and cEFIR, modified for Gauss-Markov CMN. A particle filter is used as a benchmark. It is shown that the cEFIR filter is more robust than the cEKF and almost as robust as the particle filter, although the latter is less accurate in real time.

INDEX TERMS TWOR modeling, self-localization, colored noise, extended unbiased FIR filter, extended Kalman filter.

I. INTRODUCTION

Wheeled mobile robots (WMR) are referred to as omnidirectional robotics systems that are capable of reaching every position in their environment. The first omnidirectional robot named Uranus was designed and constructed in Carnegie Melon University [1]. Since then, different kinds of such robots were exploited in industry [2], medicine, warehouses, logistics, etc. One of the most efficient types of WMR is the three-wheeled omnidirectional robot (TWOR) [3], which effectively works in indoor and outdoor environments. The TWOR has many practical advantages, such as the flexibility in travelling along complex industrial trajectories and the ability of changing the position and orientation quickly. Therefore, many efforts were made to improve TWOR modeling and control.

Since there is no standard TWOR kinematic-dynamic model yet, the authors mostly use two methodologies based on the vector approach [4] and the transformation approach [5]. The first extensive studies in this area were conducted in [6], where the kinematic model of a mobile

robot was created using the coordinate matrix transformation. Later, the Lagrange formulation was used in [7] to represent the model with reduced-order equations using a holonomy system matrix. Most recently, a cascade structure of TWORs with an inverse kinematic block was discussed in [8] to generate the velocity references required by the predictive controller. It increases the robustness to disturbances and is also better suited for multivariate problems with friction phenomena. However, this model is not well suited to model predictive control that requires accurate modeling.

In indoor environments, the TWOR self-localization can be organized using ultra wideband (UWB) technology [9] inertial navigation system (INS), hybrid schemes [10], and radio frequency identification (RFID) tags [11]. The latter approach has attracted attention due to low cost, low (or zero) energy consumption, and a wide distance range [12]. It can also be combined with other methods. For example, a novel localization method proposed in [13] combines the RFID tag data with laser-based measurements. In [14], the capabilities of a variable power RFID tags and passive ultra-high frequency (UHF) RFID tag are employed to create networks in complex environments. A localization

system designed in [15] combines two types of RFID tag-generated signals with a logical classification strategy. In [16] the authors solve the vehicle localization problem using a single antenna multi-frequency ranging scheme and compute the vehicle position through multi-parameter nonlinear optimization methods.

Regardless of the method used, the highest navigation accuracy is achieved using state estimators [17]. The Bayesian estimator developed in [15] employs process and state distributions without using a model, but is computationally inefficient. In linear Gaussian environments, the state estimation problem is optimally solved by the Kalman filter (KF). For nonlinear models, the extended KF (EKF), unscented KF (UKF), and particle filter (PF) are often used. A good robustness is offered by an unbiased finite impulse response (UFIR) filter [18] and its extended version (EFIR) [19], which do not require information of zero mean noise and initial values.

It is worth noting that RFID tag-based navigation is usually accompanied by colored measurement noise (CMN) [20], [21]. To deal with Gauss-Markov CMN, the Bryson algorithm [22] and Petovello algorithm [23] are usually used. In the Bryson algorithm, the CMN is filtered out in two phases: smoothing and filtering. In the Petovello algorithm, only one stage (filtering) is used. Most recently, several end-to-end algorithms were designed for Gauss-Markov CMN in [24] using the backward Euler method. Also, the problem with CMN was addressed by Zhou et al. in [25] using the second moment of information and by Ding et al. in [26] using the autoregressive moving average model.

In this paper, we significantly improve the TWOR non-linear model using: 1) geometric interpretation of smoothly varying velocity profiles and 2) incremental-time representation in discrete time. We also develop the EKF and EFIR filtering algorithms and modify them as cEKF and cEFIR for CMN. We show that in RFID tag environments, the cEFIR filter significantly outperforms the EFIR filter, cEKF, and EKF under CMN. The cEFIR filter is almost as robust as the PF. However, the latter is less accurate in real time. The main contributions are the following:

- An improved TWOR model for implementing hardware and software on an onboard computer.
- cEFIR and cEKF filtering algorithms for TWOR localization in CMN.
- Experimental evidence for better performance of the cEFIR filter compared to the EKF, cEKF, EFIR filter, and PF.

The rest of the paper is organized as follows. Section II develops the TWOR model with incremental-time events and formulates the problem. Section III presents the TWOR extended space-state model, modifies the equations for CMN, and develops the cEFIR, EKF, cEKF, and EFIR algorithms. Section IV provides numerical simulations with synthetic and experimental data and testes the filters for robustness. Finally, concluding remarks can be found in Section V.

FIGURE 1. Festo robotino mobile robotic development platform [27].

II. TWOR KINEMATIC AND PROBLEM FORMULATION

The TWOR manufactured as the Festo Robotino Mobile Robotic Development Platform [27] is pictured in Fig. 1. It is designed for planar motion with three degrees of freedom (DOF).

Depending on the types of dynamic constraints, TWOR can be controlled in each of the DOF independently. Such TWOR is called non-holonomic and can travel in any direction without orientation restrictions. In this paper, we are dealing with this type of TWOR.

Considering the results obtained in [5] and [6], we first modify the kinematic diagram of the TWOR with perpendicular rollers as sketched in Fig. 2.
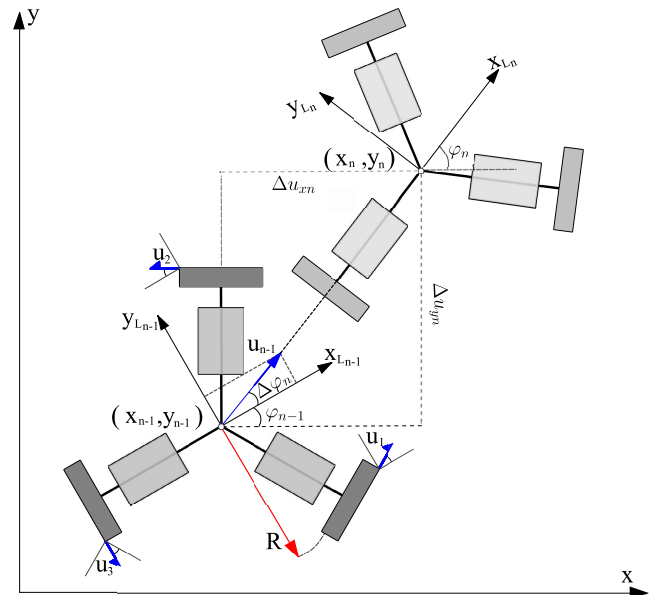

FIGURE 2. A kinematic diagram of the TWOR shown in Fig. 1.

The robot is driven by displacements in its wheels. Assuming a no-slip condition, the displacement Δu_j, $j \in [1, 3]$, in the jth wheel can be found by projecting the displacement vector u_j into the local coordinate system

(x_L, y_L) and using the contribution of the arc segment caused by the rotation $\Delta\varphi$ of the robot. This gives

$$\Delta u_j = \left\| \mathrm{proj}_{\overrightarrow{u_j}} \overrightarrow{u}_{x_L} \right\| + \left\| \mathrm{proj}_{\overrightarrow{u_j}} \overrightarrow{u}_{y_L} \right\| + \Delta\varphi * R, \quad (1)$$

where R is the radius of the robot platform. Further, we will use (1) to represent the TWOR dynamics in state space.

The problem can now be formulated as follows. Using the kinematic diagram shown in Fig. 2, we would like to represent the TWOR nonlinear dynamics in discrete-time state-space. We also wish to develop the EFIR filter, cEFIR filter, EKF, and cEKF to provide the TWOR self-localization in RFID tag environments under CMN and test them along with the PF by simulations and using experimental data.

III. STATE SPACE REPRESENTATION AND FILTERING ALGORITHMS

Looking at the kinematic diagram (Fig. 2) and considering the TWOR in two neighbouring discrete-time points, we can now represent the TWOR dynamics in nonlinear state space.

A. NONLINEAR STATE EQUATION

The TWOR reasonable state variables are u_{x_L}, u_{y_L}, and φ. Using these variables and (1), we rewrite the jth displacement $\Delta u_j, j \in [1, 3]$, in terms of the increments Δu_{x_L}, Δu_{y_L}, and $\Delta\varphi$ as

$$\begin{bmatrix} \Delta u_1 \\ \Delta u_2 \\ \Delta u_3 \end{bmatrix} = \begin{bmatrix} \cos\delta & \sin\delta & R \\ -\cos\delta & \sin\delta & R \\ 0 & -1 & R \end{bmatrix} \begin{bmatrix} \Delta u_{x_L} \\ \Delta u_{y_L} \\ \Delta\varphi \end{bmatrix}, \quad (2a)$$

$$\Delta U_i = A\Delta U_L, \quad (2b)$$

where the vector ΔU_i of displacements and the vector ΔU_L of state variables are defined by comparing (2a) and (2b), and A is a mapping matrix defined by (2a). Note that the vector ΔU_L, which contains all information about the robot location in local coordinates, can be determined in terms of ΔU_i by inverting (2b). Since the TWOR kinematics (Fig. 2) suggests that $\delta = \pi/6$, we thus have

$$\Delta U_L = A^{-1}\Delta U_i,$$
$$A^{-1} = \begin{bmatrix} \sqrt{3}/3 & -\sqrt{3}/3 & 0 \\ 1/3 & 1/3 & -2/3 \\ 1/3R & 1/3R & 1/3R \end{bmatrix}.$$

There are two ways how to represent the robot dynamics in state space. One can either assign the robot states and approximate the trajectory using a polynomial state model [10] or project the current robot position one step ahead using equations (2a) and (2b) [11], [28]. In this paper, we follow the second way as being physically more appealing.

To find the position in the global coordinate system, we introduce the discrete-time index n, apply the matrix rotation operator $R(\varphi_n)$, obtain $\Delta U = R(\varphi_n)U_L$ and $\Delta U = R(\varphi_n)A^{-1}U_i$, and provide some transformations. This gives

$$\Delta u_{xn} = \frac{\sqrt{3}}{3}\Delta u_{12n}\cos(\varphi_{n-1} + \Delta\varphi_n)$$
$$-\frac{1}{3}\Delta u_{123n}\sin(\varphi_{n-1} + \Delta\varphi_n), \quad (3)$$

$$\Delta u_{yn} = \frac{\sqrt{3}}{3}\Delta u_{12n}\sin(\varphi_{n-1} + \Delta\varphi_n)$$
$$+\frac{1}{3}\Delta u_{123n}\cos(\varphi_{n-1} + \Delta\varphi_n), \quad (4)$$

$$\Delta\varphi_n = \frac{1}{3R}(\Delta u_{1n} + \Delta u_{2n} + \Delta u_{3n}), \quad (5)$$

where $\Delta u_{12n} = \Delta u_{1n} - \Delta u_{2n}$ and $\Delta u_{123n} = \Delta u_{1n} + \Delta u_{2n} - 2\Delta u_{3n}$. In accordance with the robot odometry, Δu_{xn}, Δu_{yn}, and $\Delta\varphi_n$ are increments in the robot coordinates x and y and and heading angle φ.

The robot coordinates and heading considered as states $x_{1n} = x_{xn}$, and $x_{2n} = x_{yn}$, and $x_{3n} = \varphi_n$ at n can now be represented with the nonlinear functions

$$f_{1n} = \mathrm{x}_n = x_{1n} = x_{1(n-1)} + \Delta u_{xn},$$
$$f_{2n} = \mathrm{y}_n = x_{2n} = x_{2(n-1)} + \Delta u_{yn},$$
$$f_{3n} = \varphi_n = x_{3n} = x_{3(n-1)} + \Delta\varphi_n,$$

where the increments Δu_{xn}, Δu_{yn}, and $\Delta\varphi_n$ are given by (3)–(5). Now, for $\varphi_{n-1} = x_{3(n-1)}$, we have the following nonlinear functions with respect to the robot states,

$$f_{1n} = x_{1(n-1)} + \frac{\sqrt{3}}{3}\Delta u_{12n}\cos(x_{3(n-1)} + \Delta\varphi_n)$$
$$-\frac{1}{3}\Delta u_{123n}\sin(x_{3(n-1)} + \Delta\varphi_n), \quad (6)$$

$$f_{2n} = x_{2(n-1)} + \frac{\sqrt{3}}{3}\Delta u_{12n}\sin(x_{3(n-1)} + \Delta\varphi_n)$$
$$+\frac{1}{3}\Delta u_{123n}\cos(x_{3(n-1)} + \Delta\varphi_n) \quad (7)$$

$$f_{3n} = x_{3(n-1)} + \Delta\varphi_n. \quad (8)$$

Next, we introduce the state vector $x_n = [x_{1n}\ x_{2n}\ x_{3n}]^T$ and the control vector $u_n = [\Delta u_{1n}\ \Delta u_{2n}\ \Delta u_{3n}]^T$, whose components are variables of increments Δu_{xn}, Δu_{yn}, and $\Delta\varphi_n$ given by (6)–(8). We also suppose that the TWOR process noise is zero mean, white Gaussian, and additive and introduce the noise vector $w_n = [w_{1n}\ w_{2n}\ w_{3n}]^T \sim \mathcal{N}(0, Q)$ with the covariance $Q = E\{w_n w_n^T\}$. At this point, the TWOR dynamics can be represented in discrete-time state-space with the following nonlinear state equation

$$x_n = f(x_{n-1}, u_n) + w_n, \quad (9)$$

where the components of the nonlinear vector function $f = [f_{1n} f_{2n} f_{3n}]^T$ are specified by (6)–(8).

B. NONLINEAR OBSERVATION EQUATION

The indoor RFID tag environment can be organized with k-tags $T_j, j \in [1, k]$, having known coordinates (χ_j, μ_j, ν_j) in a way such that at least three tags are available at each n. The TWOR position can be determined via the distances d_{jn} measured between the tags and the TWOR reader in the presence of additive noise v_{jn}. The TWOR heading angle $\varphi_n = x_{3n}$ is measured in global coordinates directly by a digital gyroscope as ϕ_n in the presence of

additive noise $v_{\varphi n}$, and the observation equations can thus be written as

$$d_{1n} = \sqrt{(x_{1n} - \chi_1)^2 + (x_{2n} - \mu_1)^2 + v_1^2} + v_{1n},$$

$$d_{2n} = \sqrt{(x_{1n} - \chi_2)^2 + (x_{2n} - \mu_2)^2 + v_2^2} + v_{2n},$$

$$\vdots$$

$$d_{kn} = \sqrt{(x_{1n} - \chi_k)^2 + (x_{2n} - \mu_k)^2 + v_k^2} + v_{kn},$$

$$\phi_n = x_{3n} + v_{\varphi n}.$$

Since the RFID tag-based measurement noise in colored [20], [21], we represent v_{jn} by the Gauss-Markov model

$$v_{jn} = \Psi_j v_{j(n-1)} + \xi_{jn}, \qquad (10)$$

where $\xi_{jn} \sim \mathcal{N}(0, R_j)$ is zero mean white Gaussian driving noise with the covariance R_j and $0 < \Psi_j < 1$ is the coloredness factor, which zero value $\Psi_{jn} = 0$ makes v_{jn} white. For the sake of stability Ψ_j should not exceed unity.

The nonlinear observation equation can now be written as

$$y_n = h(x_n) + v_n, \qquad (11)$$

where $y_n = [y_{1n}\, y_{2n} \cdots y_{kn}\, y_{(k+1)n}]^T \in \mathbb{R}^{k+1}$ is the observation vector, the components of the nonlinear function $h(x_n) = [h_1(x_n)\, h_2(x_n) \ldots h_k(x_n)\, h_{k+1}(x_n)]^T$ are given by

$$h_1 = \sqrt{(x_{1n} - \chi_1)^2 + (x_{2n} - \mu_1)^2 + v_1^2},$$

$$h_2 = \sqrt{(x_{1n} - \chi_2)^2 + (x_{2n} - \mu_2)^2 + v_2^2},$$

$$\vdots$$

$$h_k = \sqrt{(x_{1n} - \chi_k)^2 + (x_{2n} - \mu_k)^2 + v_k^2},$$

$$h_{k+1} = x_{3n}$$

and the CMN $v_n = [v_{1n}\, v_{2n} \ldots v_{kn}\, v_{\varphi n}]^T \in \mathbb{R}^{k+1}$ is represented with

$$v_n = \Psi_n v_{n-1} + \eta_n, \qquad (12)$$

where $\eta_n \sim \mathcal{N}(0, R) \in \mathbb{R}^{k+1}$ is zero mean white Gaussian with the covariance R and the coloredness factor matrix $\Psi_n = \mathrm{diag}(\psi_1\, \psi_2 \ldots \psi_k\, 0)$ is diagonal.

The TWOR state-space model represented by the nonlinear equations (9), (11), and (12) can now be extended to use linear estimators as we will do next.

C. EXTENDED SPACE-STATE MODEL

The standard approach to apply linear state estimators to nonlinear models is to expand nonlinear functions $f(x_{n-1}, u_n)$ and $h(x_n)$ using the first-order Taylor series. The function $f(x_{n-1}, u_n)$ can be expanded around x_{n-1} as [19]

$$f(x_{n-1}, u_n) = f(\hat{x}_{n-1}, u_n) + F_n(x_{n-1} - \hat{x}_{n-1}) + w_n,$$

where $\hat{x}_{n-1}$ is the available past estimate and $F_n = \frac{\partial f}{\partial x}\big|_{\hat{x}_{n-1}}$ is the Jacobian matrix. The extended state equation can then be formalized with

$$x_n = F_n x_{n-1} + \tilde{u}_n + w_n, \qquad (13)$$

where $\tilde{u}_n = f(\hat{x}_{n-1}, u_n) - F_n \hat{x}_{n-1}$ is a known vector. Similarly, function $h(x_n)$ can be expanded around x_n^- as

$$h(x_n) = h(\hat{x}_n^-) + H_n(x_n - \hat{x}_n^-) + v_n,$$

where $\hat{x}_n^- \triangleq \hat{x}_{n|n-1} = F_n \hat{x}_{n-1|n-1}$ is the available prior estimate at n and $H_n = \frac{\partial h}{\partial x}\big|_{\hat{x}_n^-}$ is the Jacobian matrix.

By introducing a new observation vector $\varsigma_n = y_n - \tilde{s}_n$, where $\tilde{s}_n = h(\hat{x}_n^-) - H_n \hat{x}_n^-$ is a known function, the extended observation equation (11) attains the form

$$\varsigma_n = H_n x_n + v_n, \qquad (14)$$

where v_n is the Gauss-Markov CMN (12). The extended equations (13) and (14) can further be modified for CMN using measurement differencing as in the following.

D. EXTENDED MODEL FOR CMN

By introducing a new observation z_n, using measurement differencing, and following [24], we obtain

$$\begin{aligned} z_n &= \varsigma_n - \Psi_n \varsigma_{n-1} \\ &= H_n x_n + v_n - \Psi_n H_{n-1} x_{n-1} - \Psi_n v_{n-1} \\ &= H_n x_n + v_n - \Psi_n v_{n-1} \\ &\quad - \Psi_n H_{n-1}(F_n^{-1} x_n - F_n^{-1} w_n - F_n^{-1} \tilde{u}_n) \\ &= D_n x_n + \Gamma_n \tilde{u}_n + \bar{v}_n, \qquad (15) \end{aligned}$$

where $D_n = H_n - \Gamma_n$ and

$$\Gamma_n = \Psi_n H_{n-1} F_n^{-1}, \qquad (16)$$

$$\bar{v}_n = \Gamma_n w_n + \eta_n. \qquad (17)$$

Next, we remove the bias error from (15) as $\bar{z}_n = z_n - \Gamma_n \tilde{u}_n$, where $\Gamma_n \tilde{u}_n$ is known. This gives a new observation equation

$$\bar{z}_n = D_n x_n + \bar{v}_n, \qquad (18)$$

in which, as required, $\bar{v}_n$ is white Gaussian with the properties

$$E\{\bar{v}_n \bar{v}_n^T\} = \Gamma_n Q_n \Gamma_n^T + R_n, \qquad (19)$$

$$E\{\bar{v}_n w_n^T\} = \Gamma_n Q_n, \qquad (20)$$

$$E\{\bar{w}_n v_n^T\} = Q_n \Gamma_n^T. \qquad (21)$$

As can be seen, $\bar{v}_n$ is correlated with w_n. To apply the EKF, a new Kalman gain is required for time-correlated $\bar{v}_n$ and w_n.

E. EXTENDED KALMAN FILTER FOR CMN

To derive the Kalman gain for time-correlated w_n and $\bar{v}_n$, we define the estimation error as $\epsilon_n = x_n - \hat{x}_n$ and the prior estimation error as $\epsilon_n^- = x_n - \hat{x}_n^-$, where $\hat{x}_n^-$ is the prior estimate of x_n. Next, we follow [24] and consider the following functions: the prior error covariance $P_n^- = E\{\epsilon_n^- \epsilon_n^{-T}\}$,

$$P_n^- = F_n P_{n-1} F_n^T + Q_n, \qquad (22)$$

the measurement residual $\bar{s}_n = \bar{z}_n - D_n \hat{x}_n^-$,

$$s_n = D_n F_n \epsilon_{n-1} + D_n w_n + \bar{v}_n, \qquad (23)$$

the innovation covariance $\bar{S}_n = E\{\bar{s}_n \bar{s}_n^T\}$ obtained using (23),

$$S_n = D_n P_n^- D_n^T + H_n Q_n \Gamma_n^T + \Gamma_n Q_n D_n^T + R_n, \quad (24)$$

where $\Gamma_n = H_n - D_n$, the estimation error

$$\epsilon_n = (I - K_n D_n) F_n \epsilon_{n-1} + (I - K_n D_n) w_n - K_n \bar{v}_n, \quad (25)$$

where I denotes the Identity matrix with appropriate dimensions. The error covariance obtained using (25) as

$$\begin{aligned}
P_n &= (I - K_n D_n) P_n^- (I - K_n D_n)^T + K_n R_n K_n^T \\
&\quad - (I - K_n D_n) Q_n \Gamma_n^T K_n^T + K_n \Gamma_n Q_n \Gamma_n^T K_n^T \\
&\quad - K_n \Gamma_n Q_n (I - K_n D_n)^T \\
&= P_n^- + K_n S_n K_n^T - (P_n^- D_n^T + Q_n \Gamma_n^T) K_n^T \\
&\quad - K_n (P_n^- D_n^T + Q_n \Gamma_n^T)^T. \quad (26)
\end{aligned}$$

Because the trace of P_n is convex, we put to zero the derivative applied to the trace of (26) with respect to the bias correction gain K_n as

$$\frac{\partial \mathrm{tr}(P_n)}{\partial K_n} = -2(P_n^- D_n^T + Q_n \Gamma_n^T) + 2 K_n S_n = 0, \quad (27)$$

whose solution gives the optimal bias correction (Kalman) gain for correlated noise,

$$K_n = (P_n^- D_n^T + Q_n \Gamma_n^T) S_n^{-1}. \quad (28)$$

Finally, substituting K_n taken from (28) into (26) gives

$$P_n = (I - K_n D_n) P_n^- - K_n \Gamma_n Q_n. \quad (29)$$

A pseudo code of the cEKF for time-correlated w_n and $\bar{v}_n$ is listed as Algorithm 1.

Algorithm 1 cEKF for Correlated w_n and $\bar{v}_n$

Data: $\varsigma_n, \hat{x}_0, u_n, \Psi_n, P_0, Q_n, R_n$
Result: $\hat{x}_n, P_n$
begin
  for $n = 1, 2, \cdots$ **do**
    $z_n = \varsigma_n - \Psi_n \varsigma_{n-1}$;
    $\hat{x}_n^- = f(\hat{x}_{n-1}, u_n)$;
    $P_n^- = F_n P_{n-1} F_n^T + Q_n$;
    $S_n = H_n P_n^- H_n^T - \Psi_n H_{n-1} F_n^{-1} (P_n^- - Q_n) H_n^T$
    $+\Psi_n H_{n-1} F_n^{-1} (P_n^- - Q_n) F_n^{-T} H_{n-1}^T \Psi_n$
    $-H_n (P_n^- - Q_n) F_n^{-T} H_{n-1}^T \Psi_n + R_n$;
    $K_n = [P_n^- H_n^T - (P_n^- - Q_n) F_n^{-T} H_{n-1}^T \Psi_n] S_n^{-1}$;
    $\hat{x}_n = \hat{x}_n^- + K_n [z_n - h(\hat{x}_n^-)]$;
    $P_n = (I - K_n H_n) P_n^-$;
    $+K_n \Psi_n H_{n-1} F_n^{-1} (P_n^- - Q_n)$;
  end
end

The algorithm requires the nonlinear functions to update the estimates and the corresponding matrices of the linearized equations.

F. EXTENDED UFIR FILTER FOR CMN

The advantage of the robust UFIR filter originally derived in [29] is that it does not require any information about the zero mean noise. The only tuning factor in this filter is the averaging horizon, which must be optimal, N_{opt}, to minimize the mean square error (MSE). To develop the UFIR filter for the nonlinear model (9) and (10) using Taylor series, we follow [18] and use the linear model (13) and (18). On the horizon $[m, n]$ of N points, from $m = n - N + 1$, the state equation (13) can be extended as [19]

$$X_{m,n} = F_{m,n} x_m + B_{m,n}(U_{m,n} + W_{m,n}), \quad (30)$$

where $X_{m,n} = [x_m^T \ x_{m+1}^T \ \cdots \ x_n^T]^T$,
$U_{m,n} = [\tilde{u}_m^T \ \tilde{u}_{m+1}^T \ \cdots \ \tilde{u}_n^T]^T$, and
$W_{m,n} = [w_m^T \ w_{m+1}^T \ \cdots \ w_n^T]^T$ are the extended vectors, the extended block matrices are

$$F_{m,n} = [I \ F_{m+1}^T \ \cdots \ (\mathcal{F}_{n-1}^{m+1})^T \ (\mathcal{F}_n^{m+1})^T]^T, \quad (31)$$

$$B_{m,n} = \begin{bmatrix} I & 0 & \dots & 0 & 0 \\ F_{m+1} & I & \dots & 0 & 0 \\ \vdots & \vdots & \ddots & \vdots & \vdots \\ \mathcal{F}_{n-1}^{m+1} & \mathcal{F}_{n-1}^{m+2} & \cdots & I & 0 \\ \mathcal{F}_n^{m+1} & \mathcal{F}_n^{m+2} & \cdots & F_n & I \end{bmatrix}, \quad (32)$$

and the product matrix is defined as

$$\mathcal{F}_r^g = \begin{cases} F_r F_{r-1} \dots F_g, & g < r+1, \\ I, & g = r+1 \\ 0, & g > r+1. \end{cases} \quad (33)$$

We assume that the initial state x_m is known, and therefore $\tilde{u}_m = 0$ and $w_m = 0$.

Similarly, by assigning the extended vectors $Y_{m,n} = [z_m^T \ z_{m+1}^T \ \cdots \ z_n^T]^T$ and $V_{m,n} = [v_m^T \ v_{m+1}^T \ \cdots \ v_n^T]^T$, the extended observation equation becomes

$$Y_{m,n} = H_{m,n} x_m + L_{m,n} U_{m,n} + G_{m,n} W_{m,n} + V_{m,n}, \quad (34)$$

where the extended block observation matrix is given by

$$H_{m,n} = \begin{bmatrix} D_m (\mathcal{F}_k^{m+1})^{-1} \\ D_{m+1} (\mathcal{F}_k^{m+2})^{-1} \\ \vdots \\ D_{n-1} F_n^{-1} \\ D_n \end{bmatrix}, \quad (35)$$

and other block matrices are specified as $L_{m,n} = D_{m,n} E_{m,n}$, $G_{m,n} = D_{m,n} B_{m,n}$, and $D_{m,n} = \mathrm{diag}(D_m \ D_{m+1} \cdots D_n)$.

The algorithm requires an initialization on a short initial horizon over a data vector $Y_{m,s}$, where $s = m + K - 1$ and K is the number of the states, and the estimate will be unbiased, if the condition $E\{x_n\} = E\{\hat{x}_n\}$ is satisfied. To specify the state $\bar{x}_s$, we sequentially project it from m to s through the nonlinear function $f(x_n)$. To obtain the unavailable state $\bar{x}_m$ during the first N points, we employ a supporting KF. We also refer to [28] and assign $G_s = I$.

Algorithm 2 cEFIR Filtering Algorithm for CMN

Data: ς_n
Result: $\hat{x}_n$
begin
    for $k = N - 1, N, \cdots$ **do**
        $m = k - N + 1, s = m + K - 1$
        $G_s = I$
        for $j = 1 : K - 1$ **do**
            $\bar{x}_{m+j} = f(\bar{x}_m)$
        end
        for $l = s + 1 : k$ **do**
            $z_l = \varsigma_l - \Psi_l \varsigma_{l-1}$
            $\hat{x}_l^- = f(\bar{x}_{l-1})$
            $G_l = [D_l^T D_l + (F_l G_{l-1} F_l^T)^{-1}]^{-1}$
            $K_l = G_l D_l^T$
            $\bar{x}_l = F_l \bar{x}_{l-1} + K_l[z_l - h(\hat{x}_l^-) + \Psi_l h(\bar{x}_{l-1})]$
        end
        $\hat{x}_n = \bar{x}_n$
    end
end

The pseudo code of the cEFIR filtering algorithms developed for CMN is listed as Algorithm 2. It is worth noting that, since the cEFIR filter ignores zero mean noise, the time-correlation between the white w_n and $\bar{v}_n$ is ignored, unlike in cEKF. To determine N_{opt} in the MSE sense [30], we first compute the error covariance of the cEFIR filter by (26), where we set $K_n = G_n D_n^T$,

$$P_n = P_n^- - (2P_n^- D_n^T + 2Q_n \Gamma_n^T + G_n D_n^T S_n) D_n G_n. \quad (36)$$

We then numerically find N_{opt} by minimizing the trace of (35) as shown in [30].

G. COMPUTATIONAL COMPLEXITY

In this section, we discuss the computational complexity of the estimation algorithms. We also provide a comparison of the discussed algorithms with the PF. The bottleneck of the cEKF is in the computation of the residual covariance S_n, and of the cEFIR filter in the computaiton of the gain matrix G_n. In both cases, the complexity is $O(n^3)$, in terms of floating operation point (FLOP). The efficiency in terms of FLOPS is illustrated in Table 1, where K is the number of system states, M is the number of measurements, and N_{opt} is the horizon length for the cEFIR filter. This table suggests that the EKF and cEKF filters consume the smallest time, since these filters operate on a one-step horizon. To measure the consumed time, we run the algorithms for a straight TWOR movement in a simulated environment with 10 tags. The tags are deployed with equal intervals of 0.5 m along the path at a height of 1 m above the floor. The trajectory is computed over 500 points to feed the algorithms. Note that extra parameters required by the cEFIR and PF algorithms increase the computing time. To make a correct comparison, we use the following criteria:
- Run all algorithms for $\Psi_n = 0$ to obtain near the same RMSEs.

TABLE 1. Number of FLOPs in the cEKF and cEFIR Algorithms.

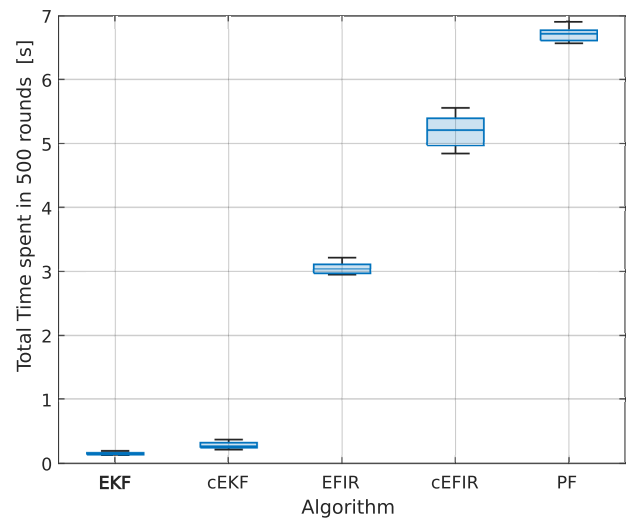| Algorithm	Transition State Function	Measurement Function	Iterative algorithm
cEKF	1	1	$9K^3 + 10K^2M$ $+5MK^2 + M^2 + 4M^3$
cEFIR	$K - 1 + N_{\text{opt}}$	N_{opt}	$N_{\text{opt}}(4K^3 + 4M^2K$ $+2K^2 + 2M^3)$

FIGURE 3. Time consumed by the filtering algorithms.

- Set the horizon N_{opt} such that the RMSEs of the cEFIR filter and cEKF become near equal.
- Run the PF with the number of particles equal to N_{opt}.

The measured computation time is shown in Fig. 3. We see that the proposed cEFIR algorithm requires more time than the cEKF, and that the PF is the slowest filter. We also see that the computation time increases from 0.108 s in the EKF to 0.2848 s in the cEKF filter, 3.0521 s in the EFIR filter, 5.1906 s in the cEFIR filter, and 6.7301 s in the PF. It is worth noting that, as a compensation for the large computation time, the filter becomes more robust that we will see in the next section.

IV. SELF-LOCALIZATION IN RFID-TAG ENVIRONMENTS

We now simulate the TWOR self-localization in RFID tag environments using the cEKF and cEFIR filter along with the EKF, EFIR filter, and PF. When no data arrive from a tag, the covariance of the measurement noise is set large, and the filter ignores this measure. In this case, lost data are replaced by prediction organized using the observation model and previously estimated state. Thereby, the observation vector always has the same dimention. To test an estimator for

robustness against CMN when the coloredness factor ranges as $0.05 \leqslant \Psi \leqslant 0.95$ with a step 0.05, we consider two scenarios of filter tuning: 1) tuning to $\Psi = 0.05$ and 2) tuning to $\Psi = 0.95$. For the FIR filters, we additionally measure the optimal horizon N_{opt} as function of Ψ. To find N_{opt}, we compute the RMSE for different values of N and choose $N = N_{\text{opt}}$ that corresponds to the minimum RMSE. The number of particles for the PF is set equal to N_{opt}.

It is worth noting that multipath effects affect RF measurements when there is no direct path between a tag and an antenna. This condition is know as Non-line-of-Sight (NLOS). The effect of NLOS reduces the effective power of the transmitted signal, leading to a biased value of Received Signal Strength Intensity (RSSI). These phenomena are main causes of tracking error in our experiment.

In what follows, we provide two investigations. In the first case, we test the filters by the TWOR circular trajectory in an indoor space with a constant motor displacement and measurement noise. In the second case, all filters are tested by experimental data available from [31].

A. CIRCULAR TRAJECTORY IN INDOOR ENVIRONMENT

The RFID tag network and the TWOR planned circular trajectory in an indoor navigation space are shown in Fig. 4a, where colored blocks represent furniture. RFID tag-based measurements corrupted by CMN with $\Psi = 0.95$ are depicted with $\times$, and we notice that multipath channels affect the measurements. We use 12 long-range UHF RFID tags (Chip Alien H3, Protocols ISO18000-6B/C, Dimensions: $78 \times 30 \times 8$ mm). The center of the RFID ALR8698 antennas is located at 0.5 m from the floor, and the RFID tags are located 1 m above the center of the antennas. All tags are spaced 2 m apart and attached to the walls in a square room (8×8)m. Each tag has a unique ID number and exactly known coordinates of location. We use a custom-build TWOR that operates based on an Nvidia Jetson TX2 board and has a radius of $R = 0.18$ m. The interrogator ALR-F800 (Alien Technology) interacts with the tags within the reader range, collects data, and transmits data to a host computer. The reader interrogation velocity is 1000 tags per second, but we employ only 12 tags. To mitigate the effect of the RFID antenna on the system performance, we use a circularly polarized antenna Alien ALR-8698. We create the observation vector using received signal strength information (RSSI) from the reader. At the test stage, we measure some RSSI values to estimate the constant parameters from the log-normal propagation model. We set the power loss coefficient for offices as $n = 33$, as recommended by Radiocommunication Sector of International Telecommunication Union ITU-R P.1238-7.

The TWOR dynamics is described by the nonlinear state space equations (9) and (11), where the number of the tags is $k = 12$. The CMN v_n in the observation (11) is modeled by the Gauss-Markov model (12), where the diagonal covariance matrix of white Gaussian noise η_n is $R = \text{diag}(\sigma_\eta^2 \dots \sigma_\eta^2 \sigma_\Phi^2)$ with $\sigma_\eta = 20$ cm and $\sigma_\Phi = \pi/360$ rad. To apply the linear filters, we use the extended
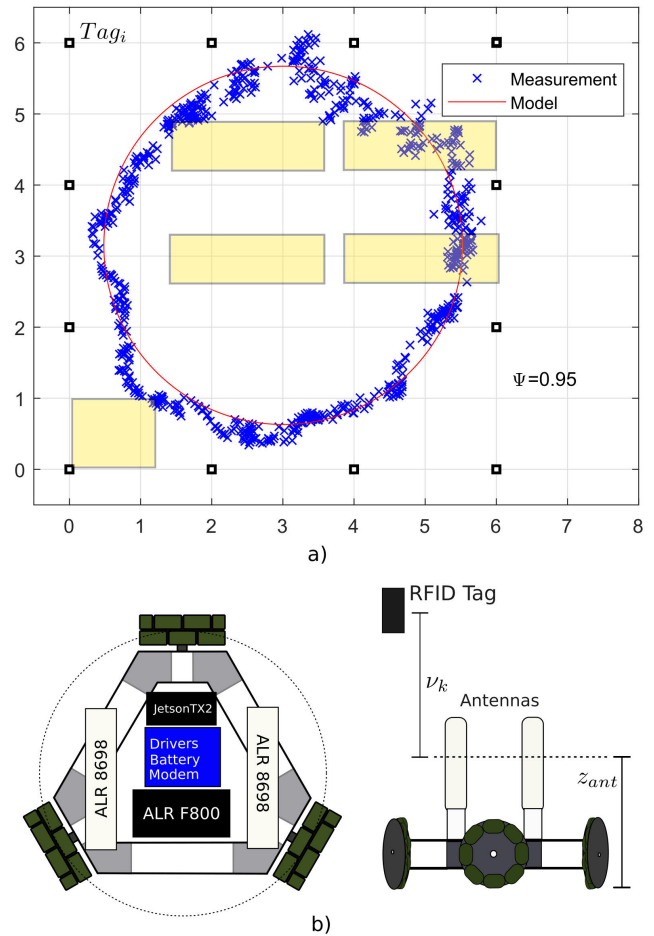

FIGURE 4. TWOR navigation in an indoor RFID environment: a) planned path and CMN-affected RFID tag-based measurements and b) TWOR design.

equations (13) and (14) and the new observation equations (15) and (18). The system noise diagonal covariance matrix $Q = \text{diag}(\sigma_w^2 \sigma_w^2 \sigma_w^2)$ has $\sigma_w = 10$ cm.

To reduce self-localization errors under CMN and test the estimators for robustness, we next conduct investigations by setting different values of the factor Ψ. To cover possible cases observed in real data, we change Ψ from 0.05 to 0.95 with a step of 0.05 and consider the following options.

1) FILTERS TUNING TO $\Psi_n = 0.05$

Before conducting this investigation, we realise that $\Psi = 0.05$ corresponds to $N_{\text{opt}} = 152$ and $\Psi = 0.95$ corresponds to $N_{\text{opt}} = 400$. Then we tune the EFIR and cEFIR filters to $\Psi = 0.05$ and $N_{\text{opt}} = 152$, and apply to the model with other values of Ψ_n. We then run the Monte Carlo (MC) simulation 100 times and show the average root MSEs (RMSEs) produced by the filters in Fig. 5. What we see is that the EFIR filters produce the smallest and consistent estimates when $\Psi < 0.5$ and that the cEKF tuned to $\Psi = 0.05$ gives slightly larger errors. Also, no significant difference between the EFIR estimates is observed when $\Psi < 0.5$. On the
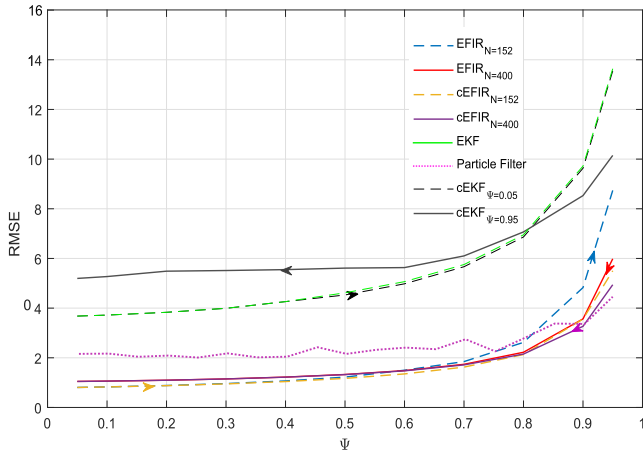
FIGURE 5. RMSEs produced by the cEKF, EFIR, cEFIR and PF algorithms.

TABLE 2. RMSEs (m) produced by EFIR and cEFIR filters with $N = 152$ and $N = 400$.

Filter	$\Psi = 0.05$		$\Psi = 0.5$		$\Psi = 0.95$	
	152	400	152	400	152	400
EFIR	0.805	1.048	1.222	1.327	8.739	5.985
cEFIR	0.805	**1.047**	**1.170**	**1.323**	**5.504**	**4.941**

TABLE 3. RMSEs (m) produced by cEKF filters for $\Psi_{opt} = 0.05; 0.95$.

Filter	$\Psi = 0.05$	$\Psi = 0.5$	$\Psi = 0.95$
cEKF($\Psi = 0.05$)	3.679	4.529	13.551
cEKF($\Psi = 0.95$)	5.195	5.610	10.148

contrary, under the heavy CMN with $\Psi = 0.95$, all filters produce large errors, although the EFIR filters give more accuracy.

The RMSEs produced by the EFIR and cEFIR filters tuned to $\Psi = 0.05$ for the process affected by $\Psi = 0.05$, $\Psi = 0.5$, and $\Psi = 0.95$ are listed in Table 2, where we test the filters by $N_{opt} = 152$ and $N = 400$ for each Ψ. The RMSEs produced by the EKF and cEKF tuned to $\Psi = 0.05$ are listed in Table 3 (first row). We see that the cEFIR filter produces the smallest errors (bolded) when $152 \leqslant N \leqslant 400$ that definitely speaks in favor of its robustness to N. The benchmark PF demonstrates the highest robustness in Fig. 5, but this filter is less accurate then the cEFIR filter.

2) FILTERS TUNING TO $\Psi_n = 0.95$

In the robust mode, we tune the filters to the worst error case of $\Psi = 0.95$ and $N_{opt} = 400$. Then we reduce Ψ in the model from 0.95 to 0.05, compute the RMSEs, and put the results to Table 2 (case of $\Psi = 0.95$ and $N_{opt} = 400$) and Table 3 (second row). No significant differences is observed here in the filter outputs when $\Psi < 0.5$, although the cEFIR filter performs a bit better. Under the weak colored noise ($\Psi = 0.05$), the EFIR and cEFIR filters perform better than the EKF and cEKF. The PF gives the smallest RMSE of 4.42 under the heavy CMN with $\Psi = 0.95$. But the cEFIR filter gives the
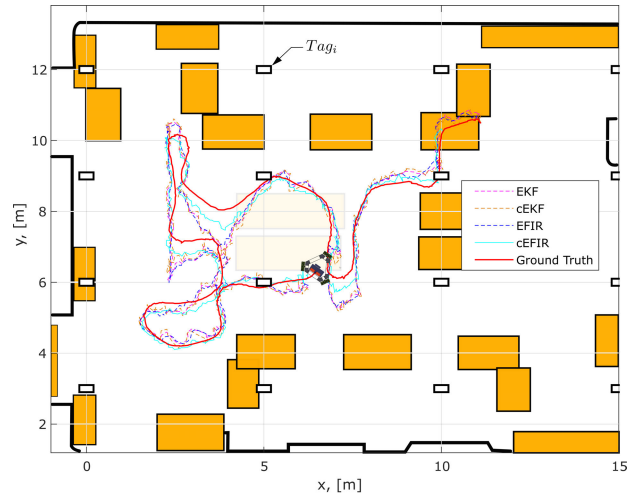

FIGURE 6. Estimation of the mobile robot trajectory in RFID tag grid environment.

TABLE 4. RMSEs (m) produced by FIR filters for $N_{opt} = 82; 245$.

Filter	$\Psi = 0.05$		$\Psi = 0.5$		$\Psi = 0.95$	
	82	245	82	245	82	245
EFIR	1.715	2.489	1.923	2.756	6.110	4.548
cEFIR	**1.712**	**2.488**	**1.910**	**2.706**	**5.131**	**4.128**

TABLE 5. RMSEs (m) produced by cEKF filters for $\Psi_{opt} = 0.05; 0.95$.

Filter	$\Psi = 0.05$	$\Psi = 0.5$	$\Psi = 0.95$
cEKF($\Psi = 0.05$)	1.753	2.093	6.407
cEKF($\Psi = 0.95$)	3.385	3.569	4.848

smaller error for smaller values of Ψ. It is worth noting that all filtering errors grow with increasing Ψ. Even so, the cEFIR filter has the lowest rate and produces the smallest average RMSE over $0.05 \leqslant \Psi \leqslant 0.95$.

B. EXPERIMENTAL TESTING

To validate the results obtained by simulations, we next consider the mobile robot experimental trajectory available from [31]. The measurement vector is created for a mesh of 16 tags placed in a square grid on a distance of 5 m to the nearest neighbor. From the dataset we take the *RFID_global_robot* fields to compute the distance to each tag in the same state-space model. To test the filters for robustness, we consider two options: 1) tuning to $\Psi = 0.05$ and 2) tuning to $\Psi = 0.95$. The workspace for the TWOR is shown in Fig.6 with the tags deployed on the floor. Also, this figure shows the estimated trajectory in the worst case of $\Psi = 0.95$.

The localization RMSEs are listed in Table 4 for EFIR and cEFIR and in Table 5 for EKF and cEKF. The RMSEs produced by the filters are sketched in Fig. 7. For filters tuned to $\Psi = 0.05$, the RMSEs are depicted with $\rightarrow$, and for $\Psi = 0.95$ with $\leftarrow$. We see that when tuned to $\Psi = 0.05$ with $N_{opt} = 82$ and to $\Psi = 0.95$ with $N_{opt} = 245$, the cEFIR filter gives the minimum errors consistent with the simulations.
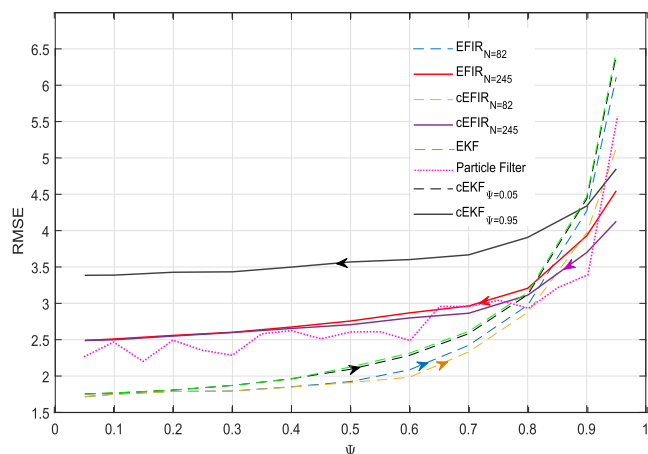
FIGURE 7. RMSEs produced by the cEKF, EFIR, cEFIR and PF algorithms.

V. CONCLUSION

The extended filtering algorithms developed in this paper have produced acceptable errors for TWOR self-localization in RFID tag indoor environments under CMN. This has become possible by improving the TWOR model using geometric interpretation for smoothly varying velocity profiles and incremental-time representation in discrete time. The results obtained by simulations and experimentally have revealed that under CMN the cEFIR filter outperforms the cEKF, EFIR filter, and EKF in terms of accuracy and robustness. The PF demonstrates a bit better robustness, but this filter is less accurate than the cEFIR filter in real time localization. It also follows that the cEFIR filter has the highest robustness under harsh operation conditions with heavy CMN. We now modify the TWOR dynamic model for linear state space representation in order to use the FIR and Kalman approaches straightforwardly. The comparative results will be reported in near future.

REFERENCES

[1] P. Muir and C. Neuman, "Kinematic modeling for feedback control of an omnidirectional wheeled mobile robot," in *Proc. IEEE Int. Conf. Robot. Autom.*, Raleigh, NC, USA, Jan. 1987, pp. 1772–1778.

[2] H.-C. Huang, "SoPC-based parallel ACO algorithm and its application to optimal motion controller design for intelligent omnidirectional mobile robots," *IEEE Trans. Ind. Informat.*, vol. 9, no. 4, pp. 1828–1835, Nov. 2013.

[3] P. F. Muir and C. P. Neuman, "Kinematic modeling of wheeled mobile robots," *J. Robotic Syst.*, vol. 4, no. 2, pp. 281–340, Apr. 1987.

[4] B.-J. Yi and W. K. Kim, "The kinematics for redundantly actuated omnidirectional mobile robots," *J. Robotic Syst.*, vol. 19, no. 6, pp. 255–267, Jun. 2002.

[5] R. Holmberg, "Design and development of powered-caster holonomic mobile robots," Ph.D. dissertation, Dept. Mech. Eng., Stanford Univ., Aug. 2000.

[6] P. F. Muir, "Modeling and control of wheeled mobile robots," Ph.D. dissertation, Dept. Mech. Eng., Stanford Univ., Carnegie Mellon Univ., Aug. 1988.

[7] S. Ostrovskaya and J. Angeles, "Nonholonomic systems revisited within the framework of analytical mechanics," *Appl. Mech. Rev.*, vol. 51, no. 7, pp. 415–433, Jul. 1998.

[8] J. C. Lins Barreto S, A. G. S. Conceicao, C. E. T. Dorea, L. Martinez, and E. R. De Pieri, "Design and implementation of model-predictive control with friction compensation on an omnidirectional mobile robot," *IEEE/ASME Trans. Mechatronics*, vol. 19, no. 2, pp. 467–476, Apr. 2014.

[9] A. R. Jimenez-Ruiz and S. F. Granja, "Comparing Ubisense, BeSpoon, and DecaWave UWB location systems: Indoor performance analysis," *IEEE Trans. Instrum. Meas.*, vol. 66, no. 8, pp. 2106–2117, Aug. 2017.

[10] Y. Xu, Y. S. Shmaliy, C. K. Ahn, T. Shen, and Y. Zhuang, "Tightly coupled integration of INS and UWB using fixed-lag extended UFIR smoothing for quadrotor localization," *IEEE Internet Things J.*, vol. 8, no. 3, pp. 1716–1727, Feb. 2021.

[11] J. J. Pomarico-Franquiz and Y. S. Shmaliy, "Accurate self-localization in RFID tag information grids using FIR filtering," *IEEE Trans. Ind. Informat.*, vol. 10, no. 2, pp. 1317–1326, May 2014.

[12] X. Liu, J. Zhang, S. Jiang, Y. Yang, K. Li, J. Cao, and J. Liu, "Accurate localization of tagged objects using mobile RFID-augmented robots," *IEEE Trans. Mobile Comput.*, vol. 20, no. 4, pp. 1273–1284, Apr. 2021.

[13] H. Wu, X. Wu, and G. Tian, "Indoor robot localization based on single RFID tag," *Artif. Life Robot.*, vol. 23, no. 3, pp. 373–379, Sep. 2018.

[14] H. Chen, X. Ai, K. Lin, N. Yan, Z. Wang, N. Jiang, and J. Yu, "BFVP: A probabilistic UHF RFID tag localization algorithm using Bayesian filter and a variable power RFID model," *IEEE Trans. Ind. Informat.*, vol. 1, no. 18, pp. 345–355, Jan. 2022.

[15] B. Tao, H. Wu, Z. Gong, Z. Yin, and H. Ding, "An RFID-based mobile robot localization method combining phase difference and readability," *IEEE Trans. Autom. Sci. Eng.*, vol. 18, no. 3, pp. 1406–1416, Jul. 2021.

[16] R. Chen, X. Huang, Y. Zhou, Y. Hui, and N. Cheng, "UHF-RFID-based real-time vehicle localization in GPS-less environments," *IEEE Trans. Intell. Transp. Syst.*, vol. 23, no. 7, pp. 9286–9293, Jul. 2022.

[17] Y. S. Shmaliy and S. Zhao, *Optimal and Robust State Estimation: Finite Impulse Response (FIR) and Kalman Approaches*. New York, NY, USA: Wiley, 2022.

[18] Y. S. Shmaliy, S. Zhao, and C. K. Ahn, "Unbiased finite impulse response filtering: An iterative alternative to Kalman filtering ignoring noise and initial conditions," *IEEE Control Syst. Mag.*, vol. 37, no. 5, pp. 70–89, Oct. 2017.

[19] Y. S. Shmaliy, "Suboptimal FIR filtering of nonlinear models in additive white Gaussian noise," *IEEE Trans. Signal Process.*, vol. 60, no. 10, pp. 5519–5527, Oct. 2012.

[20] C. Jing, T. Sun, Q. Chen, M. Du, and J. Wang, "A robust noise mitigation method for the mobile RFID location in built environment," *Sensors*, vol. 19, no. 9, pp. 1–16, 2019.

[21] K. E. Sundstrom, P. Dietrich, C. J. Diorio, and A. Friefeld, "RFID readers mitigating colored noise," U.S. Patent 8 325 014, Dec. 4, 2012.

[22] A. Bryson and L. Henrikson, "Estimation using sampled data containing sequentially correlated noise," *J. Spacecraft Rockets*, vol. 5, no. 6, pp. 662–665, 1968.

[23] M. G. Petovello, K. O'Keefe, G. Lachapelle, and M. E. Cannon, "Consideration of time-correlated errors in a Kalman filter applicable to GNSS," *J. Geodesy*, vol. 83, no. 1, pp. 51–56, Jan. 2009.

[24] Y. S. Shmaliy, S. Zhao, and C. K. Ahn, "Kalman and UFIR state estimation with coloured measurement noise using backward Euler method," *IET Signal Process.*, vol. 14, no. 2, pp. 64–71, Apr. 2020.

[25] Z. Zhou, J. Wu, Y. Li, H. Fu, and C. A. Fourati, "Critical issues on Kalman filter with colored and correlated system noises," *Asian J. Control*, vol. 19, no. 6, pp. 1905–1919, 2017.

[26] F. Ding, D. Meng, J. Dai, Q. Li, A. Alsaedi, and T. Hayat, "Least squares based iterative parameter estimation algorithm for stochastic dynamical systems with ARMA noise using the model equivalence," *Int. J. Control, Autom. Syst.*, vol. 16, no. 2, pp. 630–639, Apr. 2018.

[27] X. Nan and X. Xiaowen, "Robot experiment simulation and design based on Festo Robotino," in *Proc. IEEE 3rd Int. Conf. Commun. Softw. Netw.*, May 2011, pp. 160–162.

[28] J. J. Pomarico-Franquiz, S. Khan, and Y. S. Shmaliy, "Combined extended FIR/Kalman filtering for indoor robot localization via triangulation," *Measurement*, vol. 50, pp. 236–242, Apr. 2014.

[29] Y. S. Shmaliy, "An iterative Kalman-like algorithm ignoring noise and initial conditions," *IEEE Trans. Signal Process.*, vol. 59, no. 6, pp. 2465–2473, Jun. 2011.

[30] F. Ramirez-Echeverria, A. Sarr, and Y. S. Shmaliy, "Optimal memory for discrete-time FIR filters in state-space," *IEEE Trans. Signal Process.*, vol. 62, no. 3, pp. 557–561, Feb. 2014.

[31] P. Vorst, A. Koch, and A. Zell, "Efficient self-adjusting, similarity-based location fingerprinting with passive UHF RFID," in *Proc. IEEE Int. Conf. RFID-Technol. Appl.*, Sep. 2011, pp. 160–167.

JORGE A. ORTEGA-CONTRERAS was born in Mexico, in 1985. He received the B.S. degree in mechatronics and the M.E. degree in electrical engineering from the Universidad de Guanajuato, Salamanca, Mexico, in 2009 and 2019, respectively, where he is currently pursuing the Ph.D. degree in electrical engineering with the School of Engineering. His current research interests incude robot modeling and localization, optimal and robust filtering, and stochastic signal processing.

OSCAR G. IBARRA-MANZANO (Member, IEEE) was born in Mexico, in 1968. He received the B.S. degree in communications and electronics and the M.E. degree in electrical engineering from the Universidad de Guanajuato, Salamanca, Mexico, in 1990 and 1992, respectively, and the Ph.D. degree in electrical engineering from the National Institute for Astrophysics Optics and Electronics, Puebla, Mexico, in 1999. In 1991, he joined the Universidad de Guanajuato. He has been a Full Professor and the Chair of the Electronics Engineering Department, since 2000. From 2003 to 2012, he worked as the Dean of the Mechanical, Electrical and Electronics Engineering School, Salamanca. His current research interests include optimal estimation, adaptive filtering, and target localization.

YURIY S. SHMALIY (Fellow, IEEE) received the B.S., M.S., and Ph.D. degrees in electrical engineering from the Kharkiv Aviation Institute, Ukraine, in 1974, 1976, and 1982, respectively, and the D.C.Sc. degree in electrical engineering from the USSR Government, in 1992. From 1985 to 1999, he was with Kharkiv Military University. In 1992, he founded the Scientific Center "Sichron," and served as the Director, in 2002. Since 1999, he has been with the Universidad de Guanajuato, Mexico, where he headed the Department of Electronics Engineering, from 2012 to 2015. He has published 502 journals and conference papers and 81 patents. He has authored the books *Continuous-Time Signals* (Springer, 2006), *Continuous-Time Systems* (Springer, 2007), and *GPS-Based Optimal FIR Filtering of Clock Models* (New York: Nova Science Publications, 2009). He also edited the book *Probability: Interpretation, Theory and Applications* (New York: Nova Science Publications, 2012). He was rewarded a title, Honorary Radio Engineer of the USSR, in 1991, has received the Royal Academy of Engineering Newton Research Collaboration Program Award, in 2015, the IEEE Latin America Eminent Engineer Award, in 2021, and several best conference paper awards. He was invited many times to give tutorial, seminar, and plenary lectures. His current interests include optimal and robust state estimation with applications.

JOSÉ A. ANDRADE-LUCIO (Member, IEEE) was born in Chiapas, Mexico, in December 1969. He received the B.S. degree in communications and electrical engineering and the M.E. degree in electrical engineering from the Universidad de Guanajuato, Salamanca, Mexico, in 1993 and 1995, respectively, and the Ph.D. degree in optoelectronics sciences from the National Institute for Astrophysics Optics and Electronics, Puebla, Mexico, in 1999. Since 1999, he has been an Associate Professor, and in August 2001, he was a Titular Professor with the Department of Electrical Engineering, Universidad de Guanajuato, where he is currently the Dean of the School of Engineering. He is a member of the Mexican Academy of Sciences. His current research interests include optical signal processing, robotics, and indoor localization.

• • •